

# Hydrogen Bonding-Induced Morphology Dependence of Long-Lived Organic Room-Temperature Phosphorescence: A Computational Study

Huili Ma,<sup>†</sup> Hongde Yu,<sup>§</sup> Qian Peng,<sup>\*,‡</sup> Zhongfu An,<sup>†</sup> Dong Wang,<sup>§</sup> and Zhigang Shuai<sup>\*,§</sup>

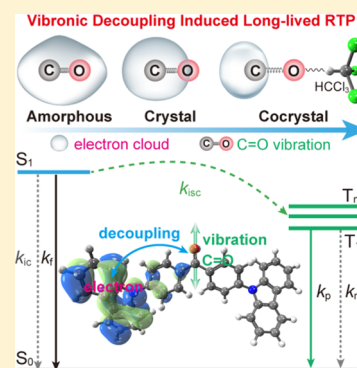
<sup>†</sup>Key Laboratory of Flexible Electronics (KLOFE) and Institute of Advanced Materials (IAM), Nanjing Tech University, Nanjing 211816, People's Republic of China

<sup>§</sup>Key Laboratory of Organic OptoElectronics and Molecular Engineering, Department of Chemistry, Tsinghua University, Beijing 100084, People's Republic of China

<sup>‡</sup>Key Laboratory of Organic Solids, Beijing National Laboratory for Molecular Science (BNLMS), Institute of Chemistry, Chinese Academy of Sciences, Beijing 100190, People's Republic of China

## Supporting Information

**ABSTRACT:** Organic room-temperature phosphorescence (RTP) is generally only exhibited in aggregate with strong dependence on morphology, which is highly sensitive to the intermolecular hydrogen bonding interaction. Here, 4,4'-bis(9*H*-carbazol-9-yl)-methanone (Cz2BP), emitting RTP in a cocrystal consisting of chloroform but not in the amorphous nor in the crystal phase, was investigated to disclose the morphology dependence through molecular dynamics simulations and first-principles calculations. We find that the strong intermolecular C=O...H-C hydrogen bonds between Cz2BP and chloroform in cocrystals decrease the nonradiative decay rate of  $T_1 \rightarrow S_0$  by 3–6 orders of magnitude due to the vibronic decoupling effect on the C=O stretching motion and the increase of ( $\pi, \pi^*$ ) composition in the  $T_1$  state. The former is responsible for high efficiency and the latter for long-lived RTP with a calculated lifetime of 208 ms (exp. 353 ms). Nevertheless, the weak hydrogen bonds cannot cause any appreciable RTP in amorphous and crystal phases. This novel understanding opens a way to design organic RTP materials.



Organic materials with persistent room-temperature phosphorescence (RTP) have aroused strong interests owing to the potential applications in bioimaging, data encryption, light emission, information display, and optical recording devices.<sup>1–8</sup> RTP from pure organic molecules always depends on aggregation morphology.<sup>9–15</sup> Even polymorphs with different molecular packing arrangements can demonstrate different RTP behaviors.<sup>10,13</sup> To date, many efforts have been devoted to elucidate the origin of aggregation morphology-dependent RTP behaviors. Several groups believed that the rigid environments in aggregates are favorable for bright organic solid-state RTP, e.g., crystals, host–guest systems, and self-assembled aggregates, owing to the restriction of molecular motions.<sup>16–25</sup> Huang and co-workers suggested that H-aggregated molecules can stabilize the triplet excitons, boosting the long-lived RTP for crystallization,<sup>26</sup> and a similar point of view was proposed by Lucenti et al. based on the investigation of the cyclic triimidazole derivatives.<sup>27</sup> Nevertheless, Li et al. claimed that  $\pi$ - $\pi$  stacking rather than H-aggregation is mainly responsible for the RTP in 10-phenyl-10*H*-phenothiazine-5,5-dioxide-based derivatives.<sup>28</sup> Chi and co-workers speculated that the intermolecular electronic coupling between the carbonyl and carbazole units enhances the intersystem crossing (ISC) rate, leading to a long-lived

RTP.<sup>29</sup> We proposed that an intermolecular electrostatic interaction can largely change the composition of the low-lying excited singlet and triplet states, leading to a controllable RTP in organic molecules that contains  $n$ -electron and  $\pi$ -electron units.<sup>30</sup> These diverse views on organic RTP indicate that it still remains a formidable challenge to reveal the intrinsic mechanism of morphology-dependent RTP.

Very recently, the importance of intermolecular hydrogen bonding interaction on RTP behaviors has come to the attention of researchers. Yuan and co-workers found that the RTP efficiency and lifetime can be promoted from aromatic esters to acids; this may be ascribed to the strong intermolecular hydrogen bonding in crystals of aromatic acids.<sup>19,31</sup> Interestingly, the RTP can also be observed in proteins,<sup>32</sup> cocrystals,<sup>9,33</sup> and self-assembled aggregates,<sup>12</sup> owing to the strong intermolecular hydrogen bond in the solid phases. Moreover, aggregation morphology is highly sensitive to the intermolecular hydrogen bonding interactions; it can vary from amorphous to crystal and even to cocrystal by involving solvent molecules.<sup>34</sup> Therefore, it is urgent to

**Received:** September 2, 2019

**Accepted:** October 25, 2019

**Published:** October 25, 2019

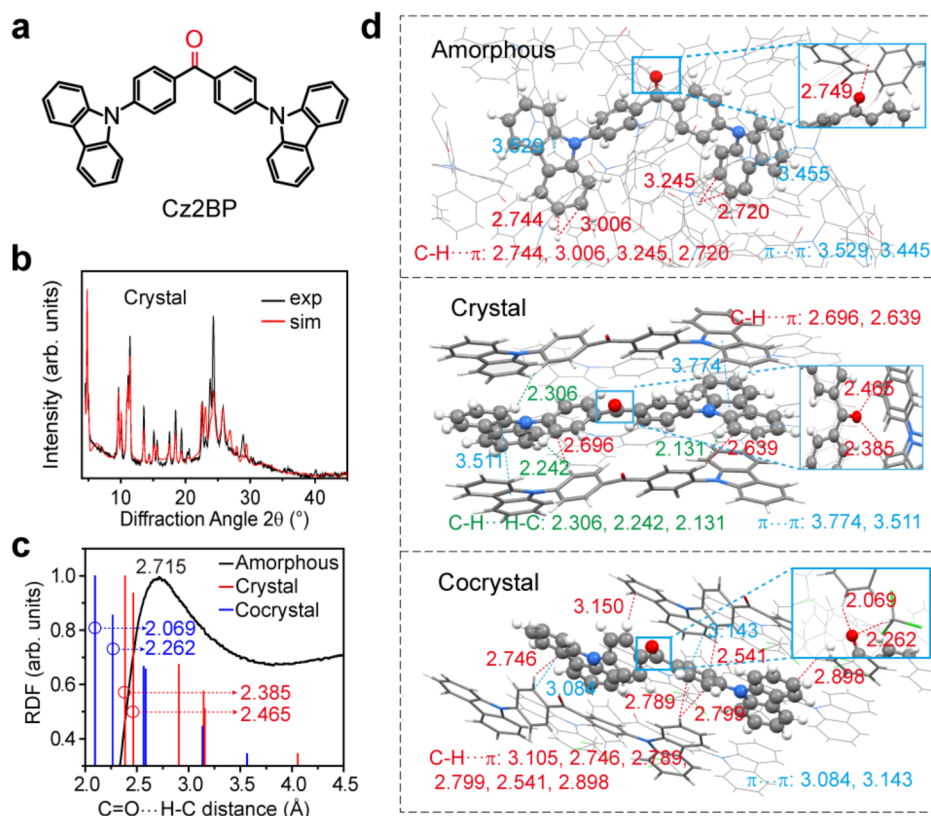


**Figure 1.** (a) Chemical structure of Cz2BP. (b) XRPD pattern of Cz2BP after refinement together with the experimental values and a difference plot. (c) Average RDFs as a function of the intermolecular C=O...H-C distance for amorphous, crystal, and cocrystal phases. (d) Perspective view of molecular packing in amorphous, crystal, and cocrystal phases for Cz2BP. The unit is angstroms ( $\text{\AA}$ ).

quantitatively expound the impact of the intermolecular hydrogen bonding interaction on morphology-dependent organic RTP.

The 4,4'-bis(9H-carbazol-9-yl)methanone (Cz2BP; see Figure 1) possesses persistent RTP ( $\tau_p = 353$  ms) in cocrystals (Cz2BP:TCM = 1:1) with chloroform (TCM) but disappears in amorphous and crystal phases.<sup>9</sup> In the Cz2BP:TCM cocrystal, there are strong intermolecular hydrogen bonds between the Cz2BP and TCM. Therefore, the Cz2BP in the amorphous, crystal, and cocrystal phases is a good prototype to quantitatively expound the dependence of RTP on the hydrogen bonding interaction. We thus take Cz2BP as an example to quantitatively calculate all of the involved excited-state decay rates involved in the RTP process by combining molecular dynamics (MD) simulations, crystal structure prediction, and time-dependent density functional theory (TDDFT) coupled with the thermal vibration correlation function (TVCF) formalism and explore the origin of the morphology-dependent RTP, especially the relationship between RTP and the intermolecular hydrogen bond strength.

**Aggregation Morphology of Cz2BP.** We first produced the amorphous Cz2BP aggregate structure by using MD simulations and then predicted the crystalline Cz2BP structure by combining Polymorph Predictor in close comparison with experimental X-ray powder diffraction (XRPD);<sup>35,36</sup> see Figures 1 and S1–S3. The MD simulations were performed with the general amber force field (GAFF) for 20 ns with a time step of 2 fs and a configuration storage period of 2 ps for statistical analysis for a cubic box of  $15 \text{ nm} \times 15 \text{ nm} \times 15 \text{ nm}$ . From Figure S4, it is seen that the volumes of Cz2BP aggregates of five trajectories quickly decrease within 1 ns and

then reach an equilibrium within 10 ns, and the structures are extracted within the final 2 ns for the analysis of the packing density and the radial distribution functions (RDFs). For crystalline Cz2BP, we prepared thousands of trial crystal structures, plotted the density of these trial structures in the  $P-1$  space group, and selected six crystal structures with lower energy and higher packing density for comparison between simulated XRPD and experimental counterparts in Figures S1–S3. Eventually, one crystal structure won out for its best match between theoretical and experimental data. Then, this crystal structure was further optimized by periodic DFT using the PBE-D3(bj) functional and refined through the Rietveld refinement algorithm, and its XRPD well reproduced the experimental one, as displayed in Figure 1b. Subsequently, the simulated amorphous and crystal structures with cell parameters  $a = 3.975 \text{ \AA}$ ,  $b = 17.725 \text{ \AA}$ ,  $c = 18.828 \text{ \AA}$ ,  $\alpha = 88.34^\circ$ ,  $\beta = 101.92^\circ$ , and  $\gamma = 82.83^\circ$  are displayed in Figure S4. In addition, the cocrystal conformation was also optimized using the PBE-D3(bj) functional starting from the experimental one.

We then looked at the morphology (Figures 1, S4, and S5): packing density, averaged RDFs (vs the intermolecular C=O...H-C distance), packing modes, and intermolecular interaction. From amorphous to crystal to cocrystal, the packing density increased from 1.158 to 1.324 to 1.505  $\text{g/cm}^3$ , indicating that the molecular packing in the cocrystal is the densest.

We note from our previous work that excited-state composition is sensitive to the intermolecular C=O...H-C distance.<sup>30</sup> We then compute the average of RDFs for Cz2BP in three aggregates, as depicted in Figure 1c. It is noted that the

amorphous conformations are extracted within the final 2 ns. It is found that the RDFs of amorphous Cz2BP with one major peak at around 2.715 Å are larger than those of the crystal (2.385 and 2.465 Å) and cocrystal (2.069 and 2.262 Å). Five representative snapshots (A0–A4) are randomly extracted from the amorphous trajectories, in which the smallest intermolecular H-bond distances are all around the RDF peak at 2.715 Å (see Figures 1d and S5), indicating that the chosen amorphous conformations are representative. Focusing on these specific aggregates from amorphous, crystal, and cocrystal phases (Figures 1d and S5), it is seen that in the amorphous phase the molecular packings are disordered and the shortest C=O⋯H–C distance (2.977 Å for A0, 2.908 Å for A1, 3.043 Å for A2, 2.749 Å for A3, and 2.488 Å for A4; see Figures 1d and S5) is the largest, indicating a weak intermolecular interaction. For the crystalline phase, the molecular packing becomes tight, and many forms of intermolecular interaction appear (Figure 1d), such as C=O⋯H–C (2.465 and 2.385 Å), C–H⋯π (2.696 and 2.639 Å), and π⋯π (3.511 and 3.774 Å) interactions. Introduction of TCM into the crystalline phases makes the molecular arrangement more compact with a number of strong intermolecular pairs such as C–H⋯π (2.541, 2.746, 2.789, 2.799, 2.898, and 3.105 Å), π⋯π (3.084 and 3.143 Å), and C=O⋯H–C (2.069 and 2.262 Å). From the theoretical calculation, such strengthened hydrogen bonding can lead to the red shift of the C=O stretching vibration, from 1740.93 cm<sup>-1</sup> in amorphous, 1736.21 cm<sup>-1</sup> in crystal, and 1711.36 cm<sup>-1</sup> in cocrystal (Figure S6).

**Nature of the Low-Lying Excited States in Aggregates.** We then turned to look at the low-lying excited-state structure of Cz2BP, including excitation energies, natural transition orbital (NTO) contours, and the spin–orbit coupling SOC constants ( $\xi$ ) for the three aggregation states. The quantum mechanics/molecular mechanics (QM/MM) model is built as shown in Figure 2. Namely, we employ TDDFT/B3LYP/6-31G(d) to calculate the Cz2BP molecule embedded inside of a cluster of molecules modeled by the GAFF in molecular mechanics.

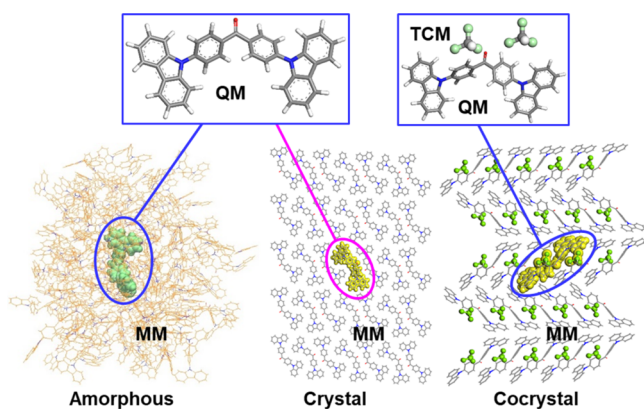


**Figure 2.** Setup of QM/MM models for Cz2BP in amorphous, crystal, and cocrystal phases.

The calculated electronic structures are shown in Figures 3 and S7–S9 and Table S1. We found that there are only two triplet states ( $T_1$  and  $T_2$ ) below the  $S_1$  state for all three cases. It is interesting that the electronic configurations of both  $S_1$  and  $T_2$  states are insensitive to environments, which are dominated by the ( $\pi$ ,  $\pi^*$ ) transitions from the  $\pi$ -orbital

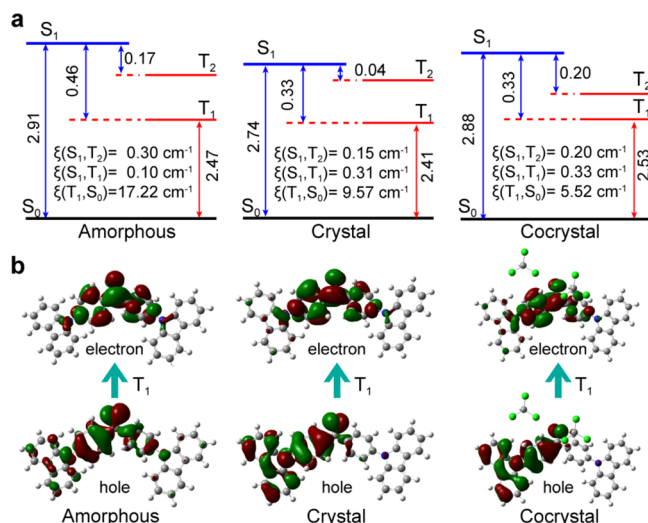


**Figure 3.** Calculated (a) energy diagram and SOC values of the low-lying excited states and (b) NTOs of  $T_1$  states for Cz2BP in amorphous, crystal and cocrystal forms. It is noted that the adiabatic excitation energy was employed.

localized on cabazole groups to the  $\pi^*$ -orbital concentrated on the diphenylketone moiety, as seen in Figures S8 and S9 and Table S1. However, for the  $T_1$  state, responsible for phosphorescence, the relative compositions of ( $n$ ,  $\pi^*$ ) and ( $\pi$ ,  $\pi^*$ ) strongly depend on the aggregation, namely, the ( $\pi$ ,  $\pi^*$ ) component in the  $T_1$  state is 59.8% in amorphous, 88.6% in crystal, and 94.6% in cocrystal, respectively. Such a trend is in line with the results that the SOC coefficients  $\xi$  of  $S_1 \rightarrow T_n$  ( $n = 1, 2$ ) are all small (less than 0.33 cm<sup>-1</sup>) in the three phases, while  $\xi$  for  $T_1 \rightarrow S_0$  decreases from 17.22 cm<sup>-1</sup> in amorphous, 9.57 cm<sup>-1</sup> in crystal, to 5.52 cm<sup>-1</sup> in cocrystal. In addition, the calculated vertical excitation energies of  $S_1$  (2.62–2.81 eV) for amorphous structures (A0–A4) are consistent with the experimental value (2.71 eV); see Table S2.

**Excited-State Conversion and Decay Rates.** To give a quantitative understanding of the aggregation-induced RTP, the excited-state conversion rates of  $S_1 \rightarrow T_{1/2}$  and decay rates of  $T_1/S_1 \rightarrow S_0$  were evaluated by using the TVCF formalism in our home-built MOMAP program,<sup>37</sup> and the results are depicted in Table 1. In TVCF, the radiative rate is evaluated by the Einstein spontaneous emission relationship, and the nonradiative rate is based on the Fermi Golden Rule with both the nonadiabatic coupling term and SOC term as the first-order perturbation in a time-dependent formalism. For the three aggregation phases, the intersystem crossing rate constants ( $k_{isc}$ ) of  $S_1 \rightarrow T_2$  and  $S_1 \rightarrow T_1$  all fall into the range of  $\sim 10^6$ – $10^7$  s<sup>-1</sup>, being comparable to the corresponding radiative decay rate constants ( $k_p$ ) of  $S_1 \rightarrow S_0$  at  $\sim 10^7$  s<sup>-1</sup>, which indicates that the triplet excitons can efficiently be populated. Subsequently, it is found that the  $k_p$  of  $T_1 \rightarrow S_0$  decreases about 1 order of magnitude from  $4.78 \times 10^1$  to  $3.15 \times 10^1$  to  $1.58$  s<sup>-1</sup> due to the decreasing oscillator strength  $f$  for  $T_1$  (see Table S2). More importantly, the  $k_{nr}$  of  $T_1 \rightarrow S_0$  is largely reduced by 3–6 orders of magnitude from  $1.87 \times 10^6$  to  $5.51 \times 10^3$  to  $6.03$  s<sup>-1</sup>. It is noted that, compared to the amorphous A0, similar results for  $k_p$  and  $k_{nr}$  of  $T_1 \rightarrow S_0$  are also obtained for Cz2BP amorphous A1–A4; see Table 1. Consequently, an efficient quantum yield  $\phi_p$  (20.76%) of  $T_1 \rightarrow S_0$  was given in the cocrystal, in comparison to the extremely low  $\phi_p$  in the amorphous (<0.04%) and crystal

**Table 1.** Calculated Fluorescence Radiative Decay Rate  $k_p$ , ISC Rates  $k_{isc}$  of  $S_1 \rightarrow T_n$  ( $n = 1, 2$ ), Radiative Rate  $k_p$ , Nonradiative Decay Rate  $k_{nr}$ , and Quantum Efficiency  $\phi_p = k_p/(k_p + k_{nr})$  of  $T_1 \rightarrow S_0$ , as Well as the RTP Lifetime  $\tau_p = 1/(k_p + k_{nr})$  for Cz2BP in Amorphous (A0–A4), Crystal, and Cocrystal Forms ( $T = 300$  K) along with the Experimental Lifetime for Comparison.

$T = 300$ K	$S_1 \rightarrow S_0$	$S_1 \rightarrow T_2$	$S_1 \rightarrow T_1$	$k_p$ ( $s^{-1}$ )	$k_{nr}$ ( $s^{-1}$ )	$T_1 \rightarrow S_0$			
	$k_f$ ( $s^{-1}$ )	$k_{isc}$ ( $s^{-1}$ )	$k_{isc}$ ( $s^{-1}$ )			$\phi_p$ (%)		$\tau_p$ (ms)	
						cal.	exp.	cal.	exp.
A0	$3.57 \times 10^7$	$2.70 \times 10^7$	$1.36 \times 10^6$	$4.47 \times 10^1$	$1.87 \times 10^6$	0.002	RTP ×	0.02	
A1	$1.56 \times 10^7$			$3.06 \times 10^1$	$6.67 \times 10^4$	0.046	RTP ×	0.46	
A2	$2.76 \times 10^7$			$4.71 \times 10^1$	$2.77 \times 10^5$	0.017	RTP ×	0.17	
A3	$5.12 \times 10^7$			$4.97 \times 10^1$	$1.16 \times 10^6$	0.004	RTP ×	0.04	
A4	$2.36 \times 10^7$			$4.78 \times 10^1$	$1.30 \times 10^6$	0.004	RTP ×	0.04	
crystal	$4.43 \times 10^7$	$4.14 \times 10^6$	$2.21 \times 10^7$	$3.15 \times 10^1$	$5.51 \times 10^3$	0.57	RTP ×	5.68	
cocrystal	$7.03 \times 10^7$	$3.96 \times 10^7$	$3.24 \times 10^6$	1.58	6.03	20.76	RTP ✓	208	353

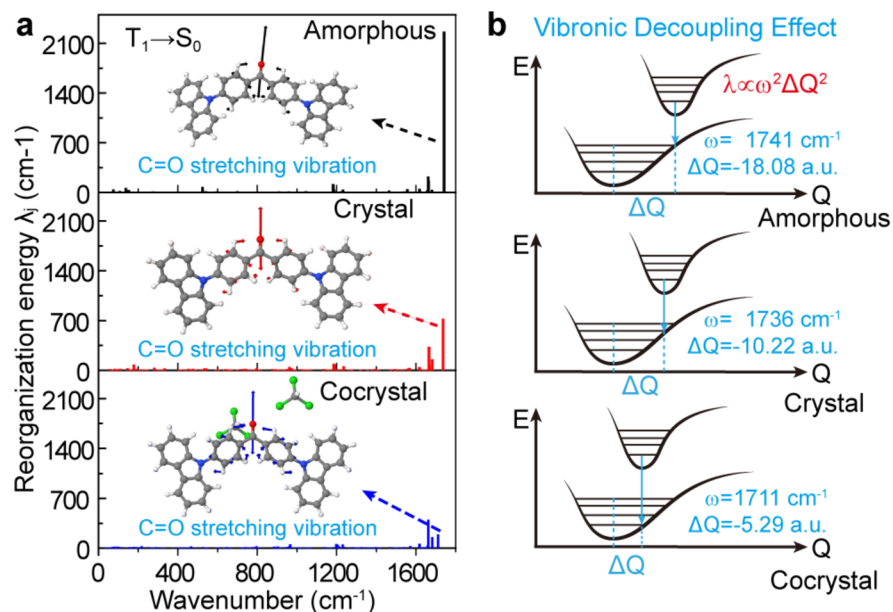


**Figure 4.** (a) Calculated normal-mode reorganization energy  $\lambda_i$  of  $T_1 \rightarrow S_0$  for amorphous, crystal, and cocrystal forms of Cz2BP. (b) Illustration of the vibronic decoupling effect of electron and C=O stretching vibration from amorphous to crystal to cocrystal. It is noted that  $\omega$  is the vibration frequency and  $\Delta Q$  is the normal-mode displacement between two states (the values of the C=O stretching vibration are listed).

phases (0.57%). On the basis of these results, it was concluded that the bright long-lived RTP of Cz2BP in the cocrystal can be attributed to the big reduction in both  $k_p$  and  $k_{nr}$  for  $T_1 \rightarrow S_0$ . This mechanism is very different from previous ones of efficient ISC to harvest the triplet exciton.<sup>12,38–41</sup> In addition, the calculated RTP lifetime  $\tau_p = 208$  ms agrees well with experimental observation of a value of 353 ms, which proved the reliability of the current theoretical models.

The ISC rate is determined by the SOC matrix  $\xi$  and the density weighted Franck–Condon factor characterized by vibronic coupling or the reorganization energy  $\lambda$ .<sup>42</sup> Because the SOC values of  $\xi(S_1, T_n)$  are small in all of the aggregates, small vibronic coupling must be responsible for the large ISC rate constants of  $S_1 \rightarrow T_2$  and  $S_1 \rightarrow T_1$ . By analyzing  $\lambda$  in Figure S10, it is observed that (i) the normal modes in the low-frequency region ( $<400$  cm<sup>-1</sup>) contribute greatly, such as the out-of-plane vibration of benzene and carbazole units with the largest  $\lambda$  of ca. 200 cm<sup>-1</sup> (inset in Figure S10); (ii) both the low-frequency and high-frequency modes contribute largely to the vibronic couplings for the  $S_1 \rightarrow T_1$  process (see Figure S10); and (iii) the vibronic couplings for  $S_1 \rightarrow T_1$  and  $S_1 \rightarrow T_2$  are all similar for the three aggregate phases, which lead to

similar ISC rate constants. The major morphology dependence lies in the SOC constant for the  $T_1 \rightarrow S_0$  process  $\xi(T_1, S_0)$ , namely, from 17.22 cm<sup>-1</sup> for amorphous, 9.57 cm<sup>-1</sup> for crystal, to 5.52 cm<sup>-1</sup> for cocrystal (see Figure 4), contributing a 1 order of magnitude decreasing nonradiative decay rate  $k_{nr}$  according to  $k_{nr} \propto \xi^2$ . The remaining 3–5 orders of magnitude decrease in  $k_{nr}$  stem from the contributions from the vibronic couplings. The calculated  $\lambda$  given in Figures 4 and S11 indicate that the reorganization energies in low-frequency modes are all negligibly small and the primary contributions to the total  $\lambda$  mainly come from the high-frequency modes ( $\sim 1600$ – $1700$  cm<sup>-1</sup>), including the stretching vibration of the C=O bond and the breathing vibration of benzene and carbazole units. More strikingly, from amorphous, crystal, to cocrystal, the reorganization energy of the C=O stretching vibration is drastically reduced from 1888.46 to 717.24 to 186.67 cm<sup>-1</sup>, with a shortened normal-mode displacement  $\Delta Q$  from  $-18.08$  to  $-10.22$  to  $-5.29$  au, mainly owing to the reduction of the C=O bond length from 0.092 to 0.064 to 0.043 Å between the  $S_0$  and  $T_1$  states (Table S3). Such a remarkable reduction is attributed to the decreased n-electron density distribution at the oxygen atom seen from the hole NTO orbital. Solvent

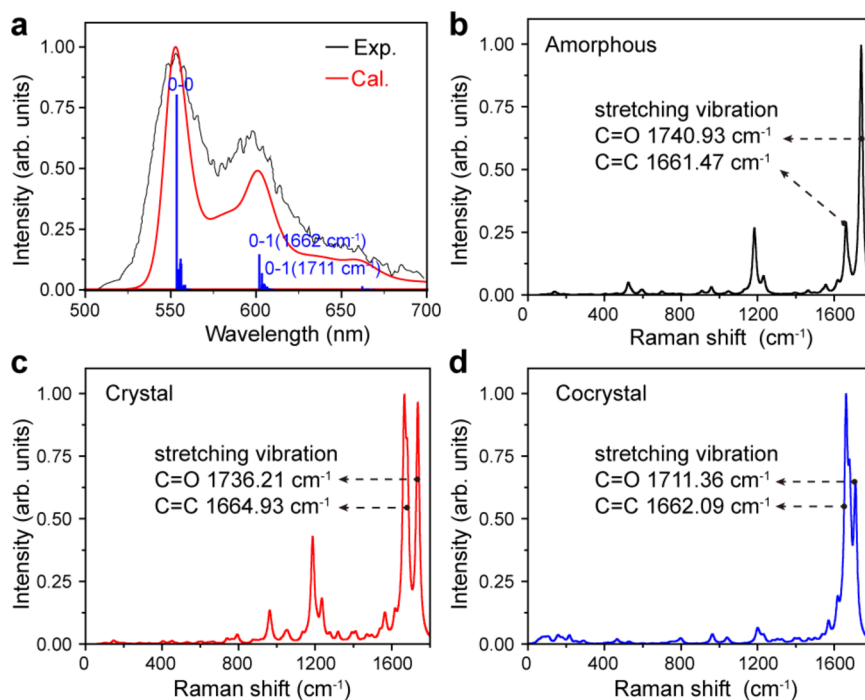


**Figure 5.** (a) Calculated phosphorescence spectra of Cz2BP in the cocrystal with a red shift of 0.14 eV to compare with the experimental ones at  $T = 300$  K. Predicted resonance Raman spectra for Cz2BP in (b) amorphous, (c) crystal, and (d) cocrystal forms by using an incident wavelength of 480 nm, Lorentz broadening of  $10\text{ cm}^{-1}$ , and a damping factor of  $100\text{ cm}^{-1}$ .

molecules TCM can move charge from carbonyl to benzene and carbazole units, as shown in Figure 3b, leading to a decoupling of the electron from the C=O stretching vibration with the decrease of the C=O bond length (see Figure 4b). It is due to such solvent-induced vibronic decoupling leading to the eventual persistent RTP!

To independently verify the above proposed mechanism, we further calculate the optical spectra. The calculated phosphorescence spectrum of Cz2BP in the cocrystal phase is in comparison with the experiment, displayed in Figure 5a. It is worthwhile to note that (i) the experimental spectra are fully reproduced by the theoretical results; (ii) the peak maximum at around 550 nm corresponds to the 0–0 transition, indicating a weak vibronic coupling; and (iii) the shoulder at  $\sim 600$  nm is mainly attributed to the 0–1 transition for the C=C and C=O stretching with  $1662$  and  $1711\text{ cm}^{-1}$ , respectively. Besides, we make theoretical predictions on the resonant Raman spectra for the three aggregate phases, as shown in Figure 5b–d, waiting for experimental verification. It is noted that the relative Raman intensity for the C=O stretching with respect to the C=C stretching mode is largely suppressed from amorphous to crystal to cocrystal phases. Such C=O stretching suppression is concomitant with an increase of the  ${}^3(\pi, \pi^*)$  proportion in  $T_1$  states.

In summary, we present a computational study on the morphology-dependent organic RTP for the Cz2BP system from the perspective of hydrogen bonding, excited-state composition, and vibronic couplings. MD simulations coupled with crystal prediction are performed to reproduce the amorphous conformations and the crystal structure. Subsequently, the QM/MM calculations are implemented to study the nature of low-lying excited states for Cz2BP in amorphous, crystal, and cocrystal phases with TCM. Eventually, the excited-state conversion and decay rates and vibrationally

resolved phosphorescence spectra are evaluated by the TVCF rate formalism in our home-built MOMAP program.

Going from amorphous to crystal to cocrystal, the intermolecular hydrogen bonding C=O $\cdots$ H–C distance is gradually decreased and makes a significant change in electron–electron and electron–vibration interactions of the low-lying excited states and determines the occurrence of the RTP. Impressively, (i) the  $T_1$  state undergoes noticeable change from the mixed ( $\pi/n \rightarrow \pi^*$ ) in amorphous and crystal phases to mainly ( $\pi \rightarrow \pi^*$ ) transition with the latter composition increasing from 59.8 to 88.6 to 94.6%; (ii) the SOC coefficients for  $S_1 \rightarrow T_2$  and  $S_1 \rightarrow T_1$  fall into the region of  $0.1\text{--}0.33\text{ cm}^{-1}$  for the three cases, but for  $T_1 \rightarrow S_0$ , they decrease sharply from 17.22 to 9.57 to  $5.52\text{ cm}^{-1}$  due to the increase of the ( $\pi \rightarrow \pi^*$ ) transition component in  $T_1$ ; (iii) the vibronic couplings are almost unchanged for  $S_1 \rightarrow T_2$  and  $S_1 \rightarrow T_1$ , while for  $T_1 \rightarrow S_0$ , they decrease drastically due to the hydrogen bond-induced charge density decrease for the C=O bond; and (iv) the ISC rate constants of  $S_1 \rightarrow T_2$  and  $S_1 \rightarrow T_1$  are on the order of  $\sim 10^6\text{--}10^7\text{ s}^{-1}$ , being comparable to the radiative rate constants of  $S_1 \rightarrow S_0$  with  $\sim 10^7\text{ s}^{-1}$ . However, the  $k_{nr}$  of  $T_1 \rightarrow S_0$  is largely reduced by 3–6 orders of magnitude from  $1.87 \times 10^6$  to  $5.51 \times 10^3$  to  $6.03\text{ s}^{-1}$ , inducing a bright and long-lived RTP with a lifetime of  $\tau_p = 208\text{ ms}$  (exp. 353 ms) for the cocrystal form. Namely, the vibronic decoupling of the electron and C=O stretching vibration caused by the strong intermolecular hydrogen bond between Cz2BP and TCM are responsible for the long-lived RTP in the cocrystal. The morphology-dependent RTP is clearly explained by the intermolecular hydrogen bond effect on both the electronic configurations and electron–vibration couplings in the  $T_1$  states. The presented results provide new insight into the RTP mechanism and a new design avenue to realize long-lived RTP by doping some small common molecules to provide strong hydrogen bonds to phosphors.

**■ ASSOCIATED CONTENT****■ Supporting Information**

The Supporting Information is available free of charge on the ACS Publications website at DOI: 10.1021/acs.jpcl.9b02568.

Computational details and results for crystal structure prediction and transition components, as well as the reorganization energy of the low-lying excited states for Cz2BP in solids and geometries and electronic structures of ground and excited states in amorphous, crystal, and cocrystal phases (PDF)

**■ AUTHOR INFORMATION****Corresponding Authors**

\*E-mail: qpeng@iccas.ac.cn. Tel: +86-10-82616830 (Q.P.).

\*E-mail: zgshuai@tsinghua.edu.cn. Tel: +86-10-62797689 (Z.S.).

**ORCID**

Huili Ma: 0000-0003-0332-2999

Qian Peng: 0000-0001-8975-8413

Zhongfu An: 0000-0002-6522-2654

Zhigang Shuai: 0000-0003-3867-2331

**Notes**

The authors declare no competing financial interest.

**■ ACKNOWLEDGMENTS**

This work is supported by the National Natural Science Foundation of China (Grant Nos. 21788102, 21973043, 21973099, 91833302, 91622121, and 21875104), the Ministry of Science and Technology of China (Grant No. 2017YFA0204501), the Strategic Priority Research Program of the Chinese Academy of Sciences (Grant No. XDB12020200), and the Natural Science Foundation of the Jiangsu Higher Education Institutions (Grant No. 19KJB150010). We are grateful to the High Performance Computing Center in Nanjing Tech University and Tsinghua University for supporting the computational resources. The authors also thank Prof. Wenjian Liu for the providing BDF software for calculating SOCs.

**■ REFERENCES**

- (1) Nicol, A.; Kwok, R. T. K.; Chen, C.; Zhao, W.; Chen, M.; Qu, J.; Tang, B. Z. Ultrafast Delivery of Aggregation-Induced Emission Nanoparticles and Pure Organic Phosphorescent Nanocrystals by Saponin Encapsulation. *J. Am. Chem. Soc.* **2017**, *139*, 14792–14799.
- (2) Fatemina, S. M. A.; Mao, Z.; Xu, S.; Yang, Z.; Chi, Z.; Liu, B. Organic Nanocrystals with Bright Red Persistent Room-Temperature Phosphorescence for Biological Applications. *Angew. Chem., Int. Ed.* **2017**, *56*, 12160–12164.
- (3) Miao, Q.; Xie, C.; Zhen, X.; Lyu, Y.; Duan, H.; Liu, X.; Jokerst, J. V.; Pu, K. Molecular afterglow imaging with bright, biodegradable polymer nanoparticles. *Nat. Biotechnol.* **2017**, *35*, 1102–1110.
- (4) Goudappagouda; Manthanath, A.; Wakchaure, V. C.; Ranjeesh, K. C.; Das, T.; Vanka, K.; Nakanishi, T.; Babu, S. S. Paintable Room-Temperature Phosphorescent Liquid Formulations of Alkylated Bromonaphthalimide. *Angew. Chem., Int. Ed.* **2019**, *58*, 2284–2288.
- (5) He, Z.; Gao, H.; Zhang, S.; Zheng, S.; Wang, Y.; Zhao, Z.; Ding, D.; Yang, B.; Zhang, Y.; Yuan, W. Z. Achieving Persistent, Efficient, and Robust Room-Temperature Phosphorescence from Pure Organics for Versatile Applications. *Adv. Mater.* **2019**, *31*, 1807222.
- (6) Wang, X.-F.; Xiao, H.; Chen, P.-Z.; Yang, Q.-Z.; Chen, B.; Tung, C.-H.; Chen, Y.-Z.; Wu, L.-Z. Pure Organic Room Temperature Phosphorescence from Excited Dimers in Self-Assembled Nano-

particles under Visible and Near-Infrared Irradiation in Water. *J. Am. Chem. Soc.* **2019**, *141*, 5045–5050.

(7) Kenry; Chen, C.; Liu, B. Enhancing the performance of pure organic room-temperature phosphorescent luminophores. *Nat. Commun.* **2019**, *10*, 2111.

(8) Zhou, Y.; Qin, W.; Du, C.; Gao, H.; Zhu, F.; Liang, G. Long-Lived Room-Temperature Phosphorescence for Visual and Quantitative Detection of Oxygen. *Angew. Chem., Int. Ed.* **2019**, *58*, 12102–12106.

(9) Li, C.; Tang, X.; Zhang, L.; Li, C.; Liu, Z.; Bo, Z.; Dong, Y. Q.; Tian, Y.-H.; Dong, Y.; Tang, B. Z. Reversible Luminescence Switching of an Organic Solid: Controllable On–Off Persistent Room Temperature Phosphorescence and Stimulated Multiple Fluorescence Conversion. *Adv. Opt. Mater.* **2015**, *3*, 1184–1190.

(10) Yang, J.; Ren, Z.; Chen, B.; Fang, M.; Zhao, Z.; Tang, B. Z.; Peng, Q.; Li, Z. Three polymorphs of one luminogen: How the molecular packing affects the RTP and AIE properties? *J. Mater. Chem. C* **2017**, *5*, 9242–9246.

(11) Xie, Y.; Ge, Y.; Peng, Q.; Li, C.; Li, Q.; Li, Z. How the Molecular Packing Affects the Room Temperature Phosphorescence in Pure Organic Compounds: Ingenious Molecular Design, Detailed Crystal Analysis, and Rational Theoretical Calculations. *Adv. Mater.* **2017**, *29*, 1606829.

(12) Bian, L.; Shi, H.; Wang, X.; Ling, K.; Ma, H.; Li, M.; Cheng, Z.; Ma, C.; Cai, S.; Wu, Q.; et al. Simultaneously Enhancing Efficiency and Lifetime of Ultralong Organic Phosphorescence Materials by Molecular Self-Assembly. *J. Am. Chem. Soc.* **2018**, *140*, 10734–10739.

(13) Zhang, T.; Zhao, Z.; Ma, H.; Zhang, Y.; Yuan, W. Z. Polymorphic Pure Organic Luminogens with Through-Space Conjugation and Persistent Room-Temperature Phosphorescence. *Chem. - Asian J.* **2019**, *14*, 884–889.

(14) Ma, H.; Lv, A.; Fu, L.; Wang, S.; An, Z.; Shi, H.; Huang, W. Room-Temperature Phosphorescence in Metal-Free Organic Materials. *Ann. Phys. (Berlin, Ger.)* **2019**, *531*, 1800482.

(15) Ma, X.; Wang, J.; Tian, H. Assembling-Induced Emission: An Efficient Approach for Amorphous Metal-Free Organic Emitting Materials with Room-Temperature Phosphorescence. *Acc. Chem. Res.* **2019**, *52*, 738–748.

(16) Baroncini, M.; Bergamini, G.; Ceroni, P. Rigidification or interaction-induced phosphorescence of organic molecules. *Chem. Commun.* **2017**, *53*, 2081–2093.

(17) Yuan, W. Z.; Shen, X. Y.; Zhao, H.; Lam, J. W. Y.; Tang, L.; Lu, P.; Wang, C.; Liu, Y.; Wang, Z.; Zheng, Q.; et al. Crystallization-Induced Phosphorescence of Pure Organic Luminogens at Room Temperature. *J. Phys. Chem. C* **2010**, *114*, 6090–6099.

(18) Bolton, O.; Lee, K.; Kim, H.-J.; Lin, K. Y.; Kim, J. Activating efficient phosphorescence from purely organic materials by crystal design. *Nat. Chem.* **2011**, *3*, 205–210.

(19) Gong, Y.; Zhao, L.; Peng, Q.; Fan, D.; Yuan, W. Z.; Zhang, Y.; Tang, B. Z. Crystallization-induced dual emission from metal- and heavy atom-free aromatic acids and esters. *Chem. Sci.* **2015**, *6*, 4438–4444.

(20) Gu, L.; Shi, H.; Bian, L.; Gu, M.; Ling, K.; Wang, X.; Ma, H.; Cai, S.; Ning, W.; Fu, L.; et al. Colour-tunable ultra-long organic phosphorescence of a single-component molecular crystal. *Nat. Photonics* **2019**, *13*, 406–411.

(21) Wei, J.; Liang, B.; Duan, R.; Cheng, Z.; Li, C.; Zhou, T.; Yi, Y.; Wang, Y. Induction of Strong Long-Lived Room-Temperature Phosphorescence of N-Phenyl-2-naphthylamine Molecules by Confinement in a Crystalline Dibromobiphenyl Matrix. *Angew. Chem., Int. Ed.* **2016**, *55*, 15589–15593.

(22) Yang, X.; Yan, D. Long-afterglow metal–organic frameworks: Reversible guest-induced phosphorescence tunability. *Chem. Sci.* **2016**, *7*, 4519–4526.

(23) Cheng, Z.; Shi, H.; Ma, H.; Bian, L.; Wu, Q.; Gu, L.; Cai, S.; Wang, X.; Xiong, W.-w.; An, Z.; Huang, W. Ultralong Phosphorescence from Organic Ionic Crystals under Ambient Conditions. *Angew. Chem., Int. Ed.* **2018**, *57*, 678–682.

- (24) Wang, Z.; Zhu, C.-Y.; Yin, S.-Y.; Wei, Z.-W.; Zhang, J.-H.; Fan, Y.-N.; Jiang, J.-J.; Pan, M.; Su, C.-Y. A Metal–Organic Supramolecular Box as a Universal Reservoir of UV, WL, and NIR Light for Long-Persistent Luminescence. *Angew. Chem., Int. Ed.* **2019**, *58*, 3481–3485.
- (25) Wu, H.; Chi, W.; Chen, Z.; Liu, G.; Gu, L.; Bindra, A. K.; Yang, G.; Liu, X.; Zhao, Y. Achieving Amorphous Ultralong Room Temperature Phosphorescence by Coassembling Planar Small Organic Molecules with Polyvinyl Alcohol. *Adv. Funct. Mater.* **2018**, *29*, 1807243.
- (26) An, Z.; Zheng, C.; Tao, Y.; Chen, R.; Shi, H.; Chen, T.; Wang, Z.; Li, H.; Deng, R.; Liu, X.; Huang, W. Stabilizing triplet excited states for ultralong organic phosphorescence. *Nat. Mater.* **2015**, *14*, 685–690.
- (27) Lucenti, E.; Forni, A.; Botta, C.; Carlucci, L.; Giannini, C.; Marinotto, D.; Pavanello, A.; Previtali, A.; Righetto, S.; Cariati, E. Cyclic Triimidazole Derivatives: Intriguing Examples of Multiple Emissions and Ultralong Phosphorescence at Room Temperature. *Angew. Chem., Int. Ed.* **2017**, *56*, 16302–16307.
- (28) Yang, J.; Zhen, X.; Wang, B.; Gao, X.; Ren, Z.; Wang, J.; Xie, Y.; Li, J.; Peng, Q.; Pu, K.; et al. The influence of the molecular packing on the room temperature phosphorescence of purely organic luminogens. *Nat. Commun.* **2018**, *9*, 840.
- (29) Yang, Z.; Mao, Z.; Zhang, X.; Ou, D.; Mu, Y.; Zhang, Y.; Zhao, C.; Liu, S.; Chi, Z.; Xu, J.; et al. Intermolecular Electronic Coupling of Organic Units for Efficient Persistent Room-Temperature Phosphorescence. *Angew. Chem., Int. Ed.* **2016**, *55*, 2181–2185.
- (30) Ma, H.; Shi, W.; Ren, J.; Li, W.; Peng, Q.; Shuai, Z. Electrostatic Interaction-Induced Room-Temperature Phosphorescence in Pure Organic Molecules from QM/MM Calculations. *J. Phys. Chem. Lett.* **2016**, *7*, 2893–2898.
- (31) Zhang, T. T.; Gao, H. Q.; Lv, A. Q.; Wang, Z. Y.; Gong, Y. Y.; Ding, D.; Ma, H. L.; Zhang, Y. M.; Yuan, W. Z. Hydrogen bonding boosted the persistent room temperature phosphorescence of pure organic compounds for multiple applications. *J. Mater. Chem. C* **2019**, *7*, 9095–9101.
- (32) Wang, Q.; Dou, X.; Chen, X.; Zhao, Z.; Wang, S.; Wang, Y.; Sui, K.; Tan, Y.; Gong, Y.; Zhang, Y.; et al. Reevaluating Protein Photoluminescence: Remarkable Visible Luminescence upon Concentration and Insight into the Emission Mechanism. *Angew. Chem., Int. Ed.* **2019**, *58*, 12667–12673.
- (33) Goswami, A.; Garai, M.; Biradha, K. Interplay of Halogen Bonding and Hydrogen Bonding in the Cocrystals and Salts of Dihalogens and Trihalides with N, N'-Bis(3-pyridylacrylamido) Derivatives: Phosphorescent Organic Salts. *Cryst. Growth Des.* **2019**, *19*, 2175–2188.
- (34) Taylor, R.; Wood, P. A. A Million Crystal Structures: The Whole Is Greater than the Sum of Its Parts. *Chem. Rev.* **2019**, *119*, 9427–9477.
- (35) Li, H.; Bahuleyan, B. K.; Johnson, R. P.; Shchipunov, Y. A.; Suh, H.; Ha, C.-S.; Kim, I. Morphology-tunable architectures constructed by supramolecular assemblies of  $\alpha$ -diimine compound: Fabrication and application as multifunctional host systems. *J. Mater. Chem.* **2011**, *21*, 17938–17945.
- (36) Beran, G. J. O. Modeling Polymorphic Molecular Crystals with Electronic Structure Theory. *Chem. Rev.* **2016**, *116*, 5567–5613.
- (37) Niu, Y.; Li, W.; Peng, Q.; Geng, H.; Yi, Y.; Wang, L.; Nan, G.; Wang, D.; Shuai, Z. MOlecular MAterials Property Prediction Package (MOMAP) 1.0: a software package for predicting the luminescent properties and mobility of organic functional materials. *Mol. Phys.* **2018**, *116*, 1078–1090.
- (38) Zhao, W.; He, Z.; Lam, J. W. Y.; Peng, Q.; Ma, H.; Shuai, Z.; Bai, G.; Hao, J.; Tang, B. Z. Rational Molecular Design for Achieving Persistent and Efficient Pure Organic Room-Temperature Phosphorescence. *Chem.* **2016**, *1*, 592–602.
- (39) Chen, X.; Xu, C.; Wang, T.; Zhou, C.; Du, J.; Wang, Z.; Xu, H.; Xie, T.; Bi, G.; Jiang, J.; et al. Versatile Room-Temperature-Phosphorescent Materials Prepared from N-Substituted Naphthalimides: Emission Enhancement and Chemical Conjugation. *Angew. Chem., Int. Ed.* **2016**, *55*, 9872–9876.
- (40) Liu, H.; Gao, Y.; Cao, J.; Li, T.; Wen, Y.; Ge, Y.; Zhang, L.; Pan, G.; Zhou, T.; Yang, B. Efficient room-temperature phosphorescence based on a pure organic sulfur-containing heterocycle: folding-induced spin–orbit coupling enhancement. *Mater. Chem. Front.* **2018**, *2*, 1853–1858.
- (41) Shi, H.; Song, L.; Ma, H.; Sun, C.; Huang, K.; Lv, A.; Ye, W.; Wang, H.; Cai, S.; Yao, W.; et al. Highly Efficient Ultralong Organic Phosphorescence through Intramolecular-Space Heavy-Atom Effect. *J. Phys. Chem. Lett.* **2019**, *10*, 595–600.
- (42) Shuai, Z.; Peng, Q. Organic light-emitting diodes: theoretical understanding of highly efficient materials and development of computational methodology. *Natl. Sci. Rev.* **2016**, *4*, 224–239.